Experiments on the effects of multiple obstacles in vented explosion chambers

Dal Jae Park [a,*], Young Soon Lee [b], Anthony Roland Green [a]

[a] *School of Safety Science, Faculty of Science, The University of New South Wales, Sydney, NSW 2052, Australia*
[b] *Department of Safety Engineering, Faculty of Engineering, Seoul National University of Technology, Seoul 139-743, Republic of Korea*

Abstract

Experimental investigations were performed to examine the effects of flame interactions with different multiple obstacles within chambers of different L/D ratios. The basic chamber consists of a rectangular box, 200 mm in height, with a 700 mm × 700 mm cross-section and a large top-venting area of 700 mm × 210 mm. The chambers were designed at 200 mm height intervals, and the maximum height of the chambers was 1000 mm. Five chambers were employed to examine the flame interaction with multiple bars in each chamber. Three different multiple obstacles were used: square, triangular and circular cross-sections with blockage ratios of 30% and 43%. The results of flame speed and pressures of different L/D ratios were discussed. The flame speeds and pressures associated with the obstacles showed little significant difference in chambers with the L/D ratios of 0.29 and 0.57. However, chambers over a ratio of 0.86 became sensitive to the obstacle types, the L/D ratio and the blockage ratios. The highest overpressures were observed with the triangular obstacles while the lowest overpressures occurred with the cylindrical obstacles. The flame development was correlated with pressure development in the chambers having L/D ratios of 0.86–1.43.
© 2007 Elsevier B.V. All rights reserved.

Keywords: Flame speed; Pressure; Obstacle types; Length to diameter ratio

1. Introduction

Over the last decade, most investigators have studied the interaction between the propagating flame and obstacles of various geometries in chambers with a large length-to-diameter ratio (L/D) such as in vessels and cylindrical tubes where L was the length of the cylinder along the direction of a propagating flame, and D was the diameter of the cylinder. With measurements in cuboid compartments, L was the height of the chamber along the direction of flame propagation, and D was the width of the chamber [1].

The Refs. [2–10] for large L/D refers the increase in flame speed and overpressure to the higher turbulence levels generated ahead of the propagating flame front by the gases interacting with the obstacles. It is well known that the interaction of the developing flow with obstacles can wrinkle the surface of a propagating flame front, and increase the flame surface area, thereby increas-

ing the burning rate. The existence of obstacles had a profound effect on flame propagation due to the generation of turbulence. The flame propagation speed was found to depend on the size and type of obstacles [7].

However, the measurements conducted in a rectangular confinement chamber with very low L/D of 0.25 by Park et al. [1] indicated an inconsistency with the literature showing that the flame speed did not increase much with blockage ratio or shape and the peak pressure showed a reverse trend to that published in the literature for large L/D. The chamber used in those experimental tests was a 1:20th scale model of governor room of the Toksan natural gas station, Korea Gas Corporation. The geometry dimensions of the enclosure are 20 m long, 19.0 wide and 4.7 m high, and it has a rectangular top-venting area of 6.4 m × 20 m. The governor room only allows venting through the roof of the room and the equipment within the room consists of pipelines, vessels, etc. that are mainly traverse to the vent axis. For the study, simplified obstacles of square, triangular and circular cross-section were used in the experiments. A more detailed explanation as to why the flame speed and the peak pressure behaved in the way it does was given by the authors in that paper. The main reason arises because the propagating

* Corresponding author. Tel.: +61 2 9385 5002; fax: +61 2 9385 6190.
E-mail addresses: d.park@student.unsw.edu.au (D.J. Park),
lysoon@snut.ac.kr (Y.S. Lee), a.green@unsw.edu.au (A.R. Green).

Table 1
Explosion chamber dimensions

Symbol	Chamber dimension (m)			Chamber volume (m³)	A_v (m²)	$A_v/V^{2/3}$	L/D
	H	W	L				
A	0.2	0.7	0.7	0.098	0.7×0.21	0.69	0.29
B	0.4	0.7	0.7	0.196	0.7×0.21	0.44	0.57
C	0.6	0.7	0.7	0.294	0.7×0.21	0.33	0.86
D	0.8	0.7	0.7	0.392	0.7×0.21	0.27	1.14
E	1.0	0.7	0.7	0.490	0.7×0.21	0.24	1.43

H: height; W: width; L: length; A_v: vent area; V: chamber volume; L/D: chamber height/chamber width.

Table 2
Distance from the bottom face of chamber to the centre of each obstacle facing the ignition point (H') within each chamber

Chambers	H' (mm)
A	70
B	200
C	300
D	400
E	500

flame was not fully developed due to the distance from ignition point to the chamber exit being too short. An increase in the chamber height is required to provide a distance over which the propagating flame could fully develop.

The main objectives in this work are to investigate the interaction between a freely propagating flame and different multiple obstacles mounted within chambers with different L/D ratios and to find out when the results obtained in the previous work [1] regain consistency with those reported in the literature in that the peak overpressure is obtained with sharp-edged obstacles such as those with triangular cross-sections and higher overpressures are obtained as the blockage ratio is increased.

2. Experimental

The fuel–air mixture, experimental procedures and equipment used in this work are the same with reported in previous work [1]. A number of explosion chambers of differing heights were used that were 700 mm × 700 mm in cross-section with a large top-venting area, A_v, of 700 mm × 210 mm. The smallest chamber was 200 mm in height and the largest was 1000 mm in height. Three other chambers were constructed at 200 mm height intervals. The five chambers were made of 20 mm thick transparent perspex. The schematic of chamber A is shown
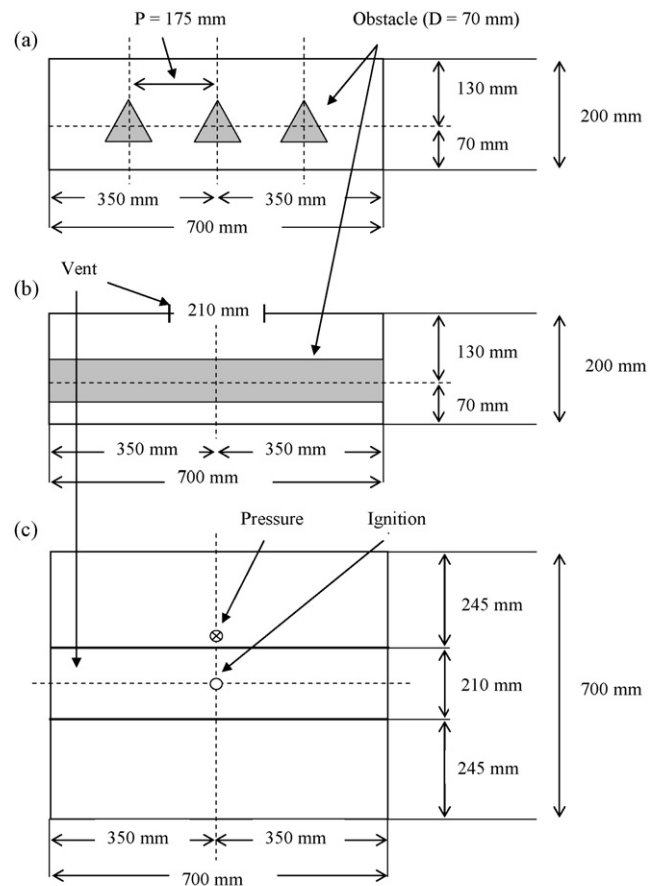

Fig. 1. Schematic for explosion chamber A: (a) front view, (b) side view and (c) top view.

Table 3
Configurations of all obstacles used in each chamber

Chambers	Obstacles	Obstacle types	Symbol	BR (%)	Dimensions (mm)
A–E	Multiple obstacles	Cylinder	MC1	30	L 700 × D 70, P = 175
			MC2	43	L 700 × D 100, P = 175
		Square	MS1	30	L 700 × S 70, P = 175
			MS2	43	L 700 × S 100, P = 175
		Triangular	MT1	30	L 700 × E.S. 70, P = 175
			MT2	43	L 700 × E.S. 100, P = 175

BR: blockage ratio, L: length, D: diameter, S: side, E.S.: equal sides, P: pitch.

Table 4
Distance from the bottom of chamber to the nearest point of the obstacle facing the ignition point (H) within each chamber

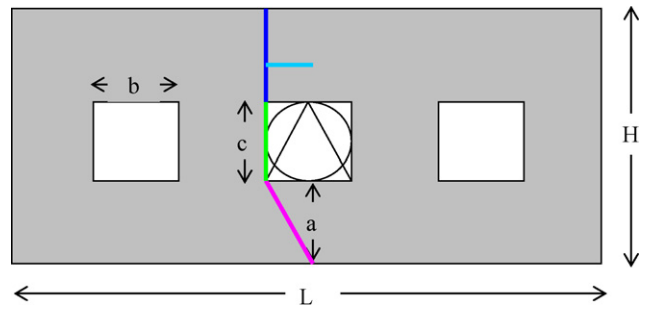| Chambers	Symbol	H (mm)
A	MC1, MS1	35
	MC2, MS2	20
	MT1	40
	MT2	27
B	MC1, MS1	165
	MC2, MS2	150
	MT1	170
	MT2	157
C	MC1, MS1	265
	MC2, MS2	250
	MT1	270
	MT2	257
D	MC1, MS1	365
	MC2, MS2	350
	MT1	370
	MT2	357
E	MC1, MS1	465
	MC2, MS2	450
	MT1	470
	MT2	457

Fig. 2. Schematic of a chamber B and obstacles dimensions used for calculating the characteristic length.

in Fig. 1. Full details of the chambers employed are given in Table 1.

The chambers were sealed with a thin plastic membrane across the vent to contain the flammable mixture prior to ignition. The bottom of the chamber remained closed and the larger rectangular vent on the top plate was covered with thin polyethylene film before gas filling. The perspex was used to allow an observation of the flame propagation by a high-speed video camera. The pressure inside the chambers was monitored by one pressure transducer mounted on the top wall of the chamber, 20 mm from the chamber exit. A methane–air concentration of 10% within
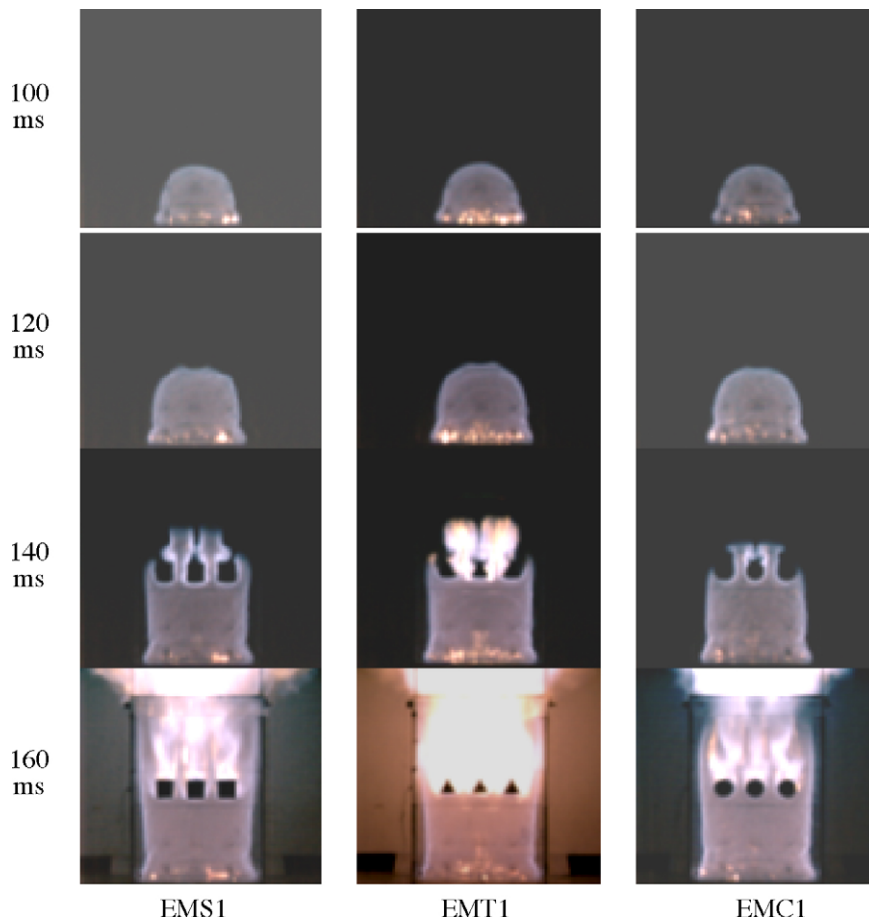

Fig. 3. Global flame propagation around different multiple cross-section obstacles with blockage ratio of 0.43 in a chamber E.

the chambers was ignited by an electric spark positioned at the centre of the bottom wall.

Three different types of multiple obstacles: cylindrical, square and triangular bars of length 700 mm, having blockage ratios of both 30% and 42.85% were placed within the chambers. All the obstacles used in each chamber were made from acrylic or wood. Obstacles were centred in the middle of the chambers, except for chamber A, the smallest chamber. In this chamber if an obstacle was placed in the middle of the chamber the flame propagation distance behind an obstacle would be too short and therefore difficult to observe. Consequently obstacles were centred 70 mm from the bottom of the chamber rather than in the centre of the chamber. The triangular obstacle is positioned slightly higher than the other two obstacle configurations, and the lower blockage ratio is positioned slightly higher than the higher blockage ratio. Full details of the configurations and locations of all obstacles used in each chamber are given in Tables 2–4.

3. Analysis techniques of local flame propagation

The analysis techniques to investigate the local flame-front characteristics are the same as previous work of Park et al. [1]. The local flame displacement speed, S_{fd}, was calculated along the flame front by dividing the distance (Δx) along the normal line at each point by the time between two consecutive flame images (Δt). Any flame fronts that touched the obstacle were uncovered from the estimation of the displacement speed. The mean flame propagation speed between two consecutive images is then determined as $\bar{S}_{fd} = \sum_{i=1}^{n} S_{fd}/n$ where n is the number of pixel points on the first flame front image. The mean flame velocity ($\bar{S}_F$) based on the mean flame displacement speed ($\bar{S}_{fd}$) estimated from the temporal evolution of the flame contours obtained by high-speed camera can be calculated as $\bar{S}_F = (\bar{\rho}_b/\rho_u) \cdot \bar{S}_{fd}$, where $\bar{\rho}_b$ the mean density of burnt gas behind the flame front, ρ_u the density of unburned mixtures [1].

A statistical method was used for each identified stage in which probability density functions (pdfs) of local flame displacement speed were calculated from all data points along the flame front within the time frame of the stage [1]. Four stages can be identified as the flame front interacts and propagates around the obstacle:

- *Stage I*: ignition to approaching the front face;
- *Stage II*: flow around the bottom face to the point where a shear wake forms (in the case of the triangular and square bars it is the corner of the bottom face, while it is the full diameter for the cylinder);
- *Stage III*: flame progression along the lateral sides of the square. This is not present for the other obstacles;
- *Stage IV*: the recirculation region behind the obstacle (from the corner of the top face for the square bar or the bottom face for the triangular bar, or the full diameter for the cylinder) until flame reconnection behind the obstacle.

Fig. 2 shows an example of a schematic diagram of obstacles employed within chamber B for calculating characteristic

length. Where H is the chamber height (=0.4 m), L is the chamber length (=0.7 m), a is the distance from the bottom of chamber to the middle point of each obstacle, b is the diameter for circle and the side length for square and triangle, and c is the height of each obstacle.

For stage I the characteristic length corresponds to a. For stage II the length is calculated as $\sqrt{(a)^2 + (b/2)^2}$ for the square and triangular bars, and $\sqrt{(a + (b/2))^2 + (b/2)^2}$ for the cylinder. Stage III is observed only in the square obstacle is a combination of stage II and c. The characteristic length in stage IV is then $\pi b/4 +$ stage II for the circular bars, $b/2 +$ stage III for the square bars, and $b +$ stage II for the triangular bars. The characteristic time is determined as the characteristic length in each stage (m)/laminar flame speed (=2.85 m/s). The non-dimensional time is calculated from the actual time of each stage/characteristic time.

4. Results and discussion

4.1. Global and local flame developments

Figs. 3 and 4 show examples of global and local flame development with three different multiple obstacles of 0.43 BR:
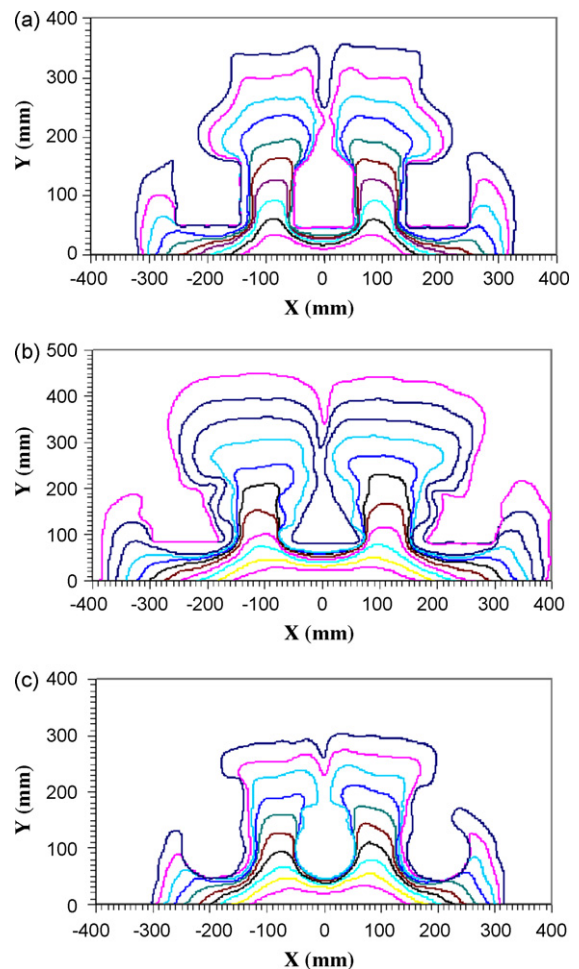

Fig. 4. Local flame propagation for different bars with a blockage ratio of 0.43 BR in the chamber E: (a) EMS2 (118–136 ms), (b) EMT2 (118–138 ms) and (c) EMC2 (118–136 ms).

circular, triangular and square cross-sections within chamber E which has a *L/D* ratio of 1.43. Subsequent global flame images at 20 ms intervals between 100 ms and 160 ms after ignition are shown in Fig. 3. The local region of interest selected here was around the multiple obstacles. Local flame propagation of the same system with flame contours at 2 ms intervals is shown in Fig. 4. The first local flame contour shown for the different obstacles is at $t = 118$ ms and the last contours are at about 136–138 ms.

The major features in the global and local contours of flame propagation around the multiple obstacles within the chamber provide an understanding of the flame development. As shown in Fig. 3, the flame develops hemispherically in a similar manner to the laminar flame from the ignition point to $t =$ approximately 100 ms with the presence of the obstacle having no apparent effect on the flame shape. During the period about $t = 100$ ms to $t = 120$ ms the flame consumes unburnt mixtures closer to the obstacle. Between these periods the flame displacement speed slows as it approaches the lower face of the central obstacle

due to the stagnation point immediately below it. As the leading flame consumes unburnt mixture closer to the lower face of the obstacle it is clearly seen that the central surface of the flame front becomes concave. As the flame front continues to develop, the central region of flame development is slowed due to the obstacle in the path of the flame resulting in the central region of the leading flame front becoming flat. This phenomena can be seen at around $t = 118$ ms in Fig. 4. For the different obstacle configurations, the travel time of the leading flame from ignition to the lower face of the obstacle was found to be similar. After the impingement on the central obstacle, the two leading flame fronts propagate downstream behind the obstacle with an increase in the flame surface area. As the flame is forced to burn through the openings between the central obstacle and side obstacles, the surface of laterally propagating flame begins to become concave due to the presence of the side obstacles. While the leading flame front continues to develop between the obstacles until flame reconnection occurs behind the central obstacle, the lateral flame front near the side obstacles contin-
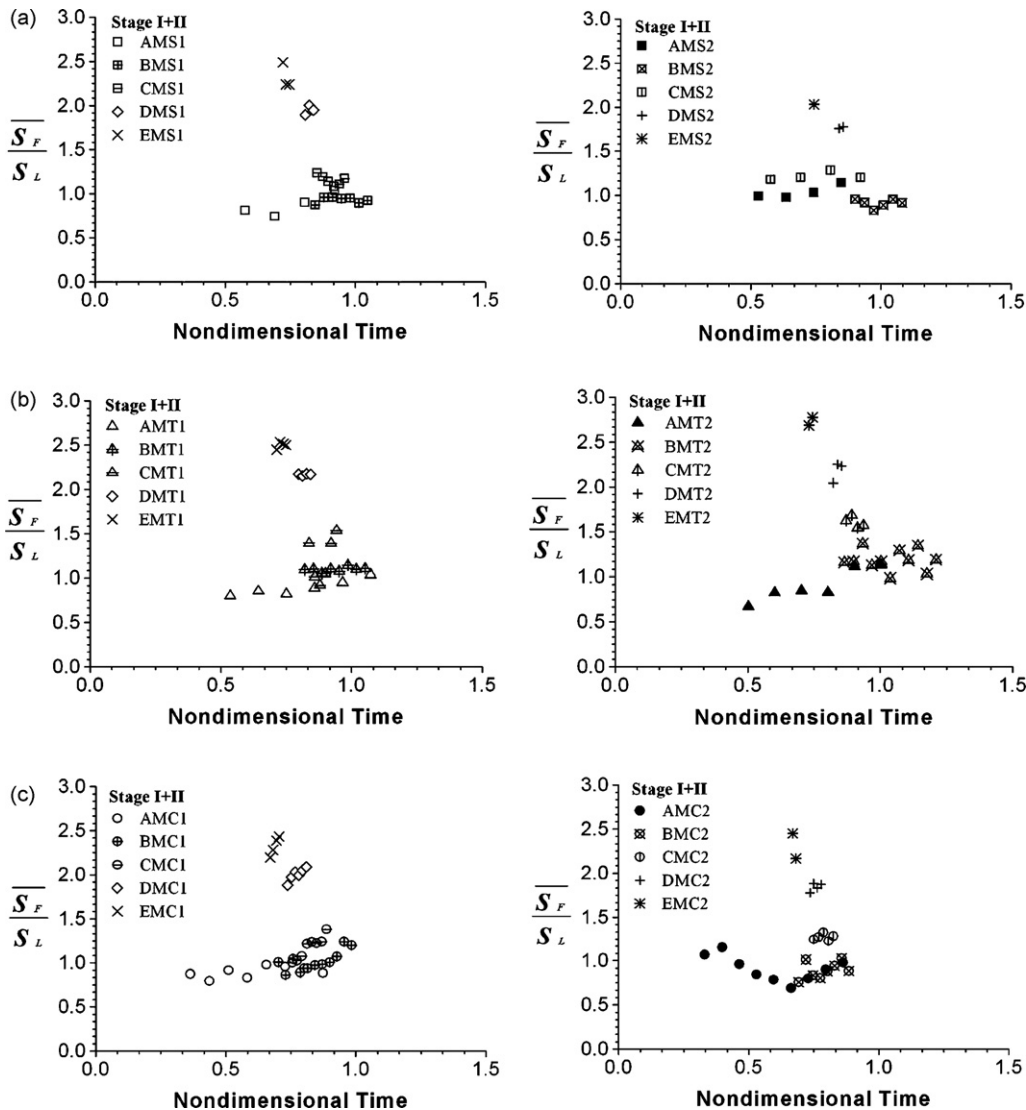

Fig. 5. The mean local flame speed during stages I + II for multiple bars of 0.3 BR and 0.43 BR in the chambers with different *L/D* ratios: (a) square, (b) triangular and (c) circular.

ues to develop in a concave nature, and this causes slower flame development in these regions. The flame reconnection in the wake of central obstacles occurred at about 134–136 ms. After about $t = 140$ ms the moving flame behind the side obstacles continues to propagate in the wake of the obstacles. With increasing time, the flame approaches the chamber exit. The triangular bars caused the shortest elapsed time to the vent, this occurred at about 144 ms while the longest time was obtained with the circular bars, this occurred at about 152 ms and demonstrates that the flame speed was accelerated more in the presence of the triangular obstacles than the other two obstacle configurations.

As the flame front reached the chamber exit, the propagating flame front moved laterally along the vent with a significant increase in flame surface area, pushing unburnt mixture ahead of it. The flame front emerging from the vent ignites the unburnt gases which have previously been expelled from the chamber. At about $t = 160$ ms the flame eventually encounters the walls of the chamber. At this point the rate of production of burned gas volume begins to decrease due to a reduction in flame area.

4.2. Flame speed at different L/D ratios

The influence of three different multiple bars of 0.3 BR and 0.4 BR: square, triangular and circular cross-sections on the mean flame speed in different *L/D* chambers is compared for stages I + II of flame development, as shown in Fig. 5. The $\bar{S}_F/S_L$ increases in stages I + II as the chamber height is increased. Here, the laminar flame speed, S_L, corresponds to $(\rho_u/\rho_b) \cdot S_L = 2.85$ m/s. The laminar burning velocity, S_l, for methane–air mixture at an equivalence ratio of $\Phi = 1.05$ used here is 0.38 m/s [11] and the density ratio across the flame, ρ_u/ρ_b, is about 7.5 [1].

The trends of $\bar{S}_F/S_L$ for three different obstacles in two chambers A and B, were similar. The mean flame speeds are found to be around 1.0, regardless of the obstacle geometries and obstruction ratios. The local flame speeds are almost equal to the laminar burning speed. However, in the other chambers, the initial flame speed was noticeably larger and increased with the height of the chamber. A relatively higher flame speed is observed with the triangular obstacles rather than other configurations. These fast initial flame speeds cause higher speeds in the unburnt gas ahead of the flame and thus creates higher turbulence downstream of the obstacle.

Fig. 6 displays the results of mean flame speed during stage III (square obstacles), and indicates the different flame interactions in the various chambers where higher flame speeds tend to correlate with higher *L/D* ratios. The pdf for the square obstacles in chamber A, shown in Fig. 7, has a narrow distribution with the peak corresponding to $S_{fd} = 2.85$ m/s. While this pdf has a longer tail at higher values than those of the previous stage with values as high as $S_{fd} = 5$ m/s, it is still relatively narrow compared to the other chambers. Any shift to higher values shown in the pdf implies turbulence levels have changed due to interaction with the shear layer turbulence along the side of the obstacle. Stage III of the larger square obstacles has a peak pdf of about 0.7 at 2.5 m/s. This is below the nominal flame speed and occurs
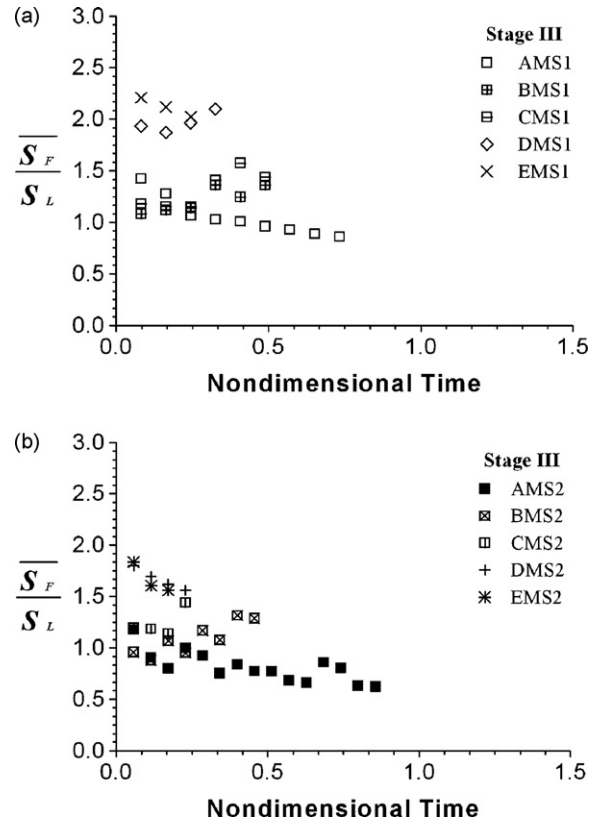

Fig. 6. The mean local flame speed during stage III for square multiple bars of 0.3 BR and 0.43 BR in the chambers with different *L/D* ratios: (a) 0.3 BR and (b) 0.43 BR.

because of flame deceleration caused by the presence of the side obstacles.

The pdfs during stage III in chamber B have a longer tail than chamber A. The leading flame front interaction with vortices generated within the shear layer on the sides of the square caused slightly larger regions where $S_{fd} > 2.85$ m/s. Chamber C has a larger portion of the pdf with $S_{fd} > 2.85$ m/s, and a smaller portion with $S_{fd} < 2.85$ m/s. Here the flame front propagating towards both sides of the left and right obstacles becomes concave, resulting in flame deceleration and increasing the proportion below 2.85 m/s. In chambers D and E the flame front along the sides of the square is even more turbulent in nature.

Fig. 8 presents the results of mean flame speed during stage IV for all obstacles in the chambers with different *L/D* ratios. Stage IV is associated with the turbulent wake regions downstream of the central obstacle. A common feature of the local displacement speed pdf in all chambers is the shorter tail towards the lower speeds ($S_{fd} < 2.85$ m/s) and the longer tail towards the higher speeds ($S_{fd} > 2.85$ m/s) compared with earlier stages. Both of these attributes are the result of flame interaction with the central and side obstacles. The distribution located in regions of the lower speed is due to the effect of a concave flame generated near the side obstacles. The broaden structure and larger proportion to higher values in the pdfs are the result of the flame interaction with the recirculating structures developed in the flow behind the central obstacle until flame reconnection occurs and is related to turbulent flame structures, with a much greater surface area.
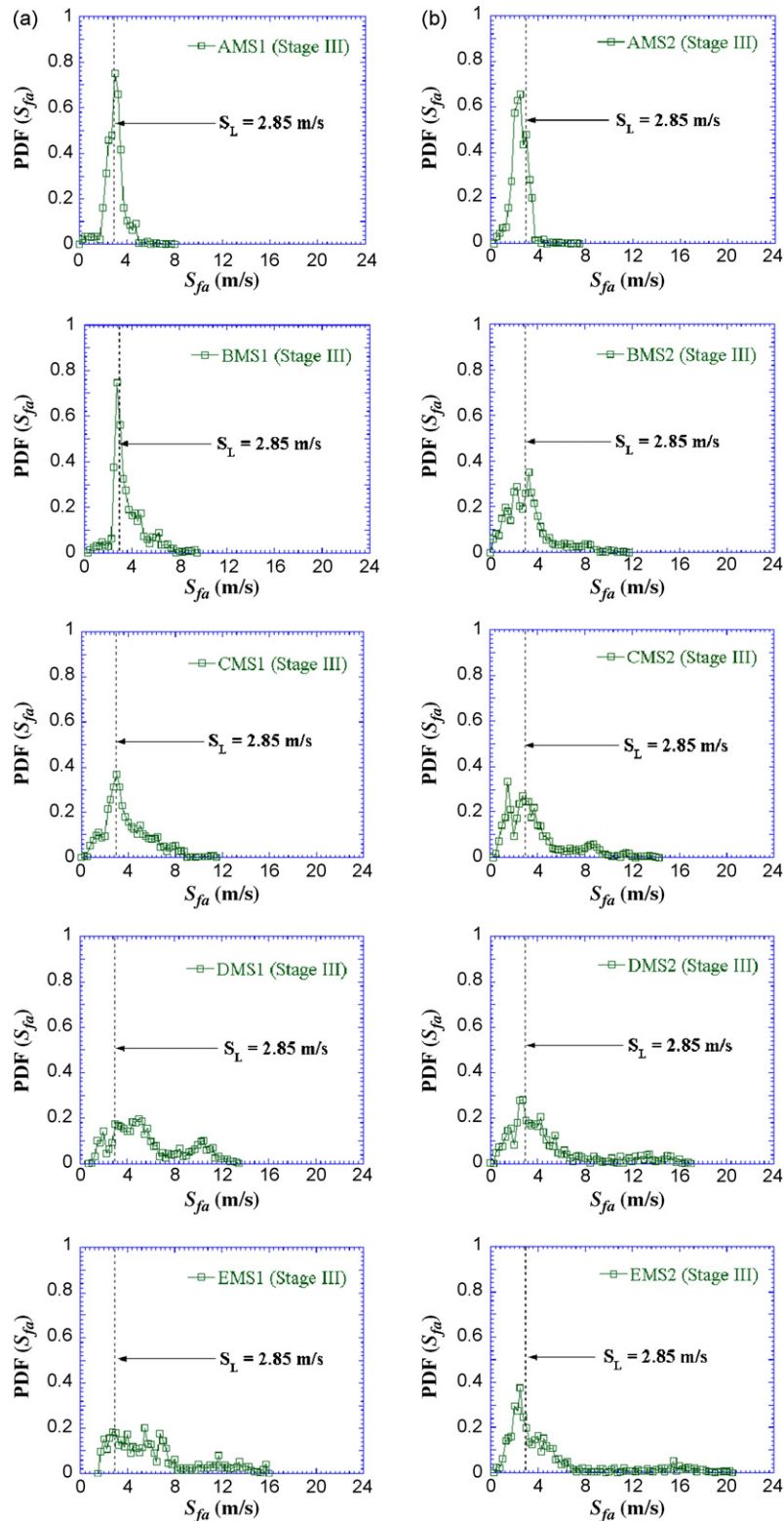
Fig. 7. PDFs of local flame displacement speed square bars at two blockage ratios during stage III in the five chambers: (a) MS1 and (b) MS2.

The existence of a concave flame generated ahead of both the central obstacle and side obstacles causes the flame deceleration. The larger obstacles (0.43 BR) have the higher proportion of the pdf below 2.85 m/s due to having a more concaved flame than that of the lower blockage ratio as the flame approaches a stagnation point. Although the speeds increased with the height of the chamber, the mean flame speed for the higher blockage ratio of 0.43 during stages I + II and III, indicates less flame stretching than is seen at 0.3. This implies the larger obstruction generates the larger concave flame structures which decelerate
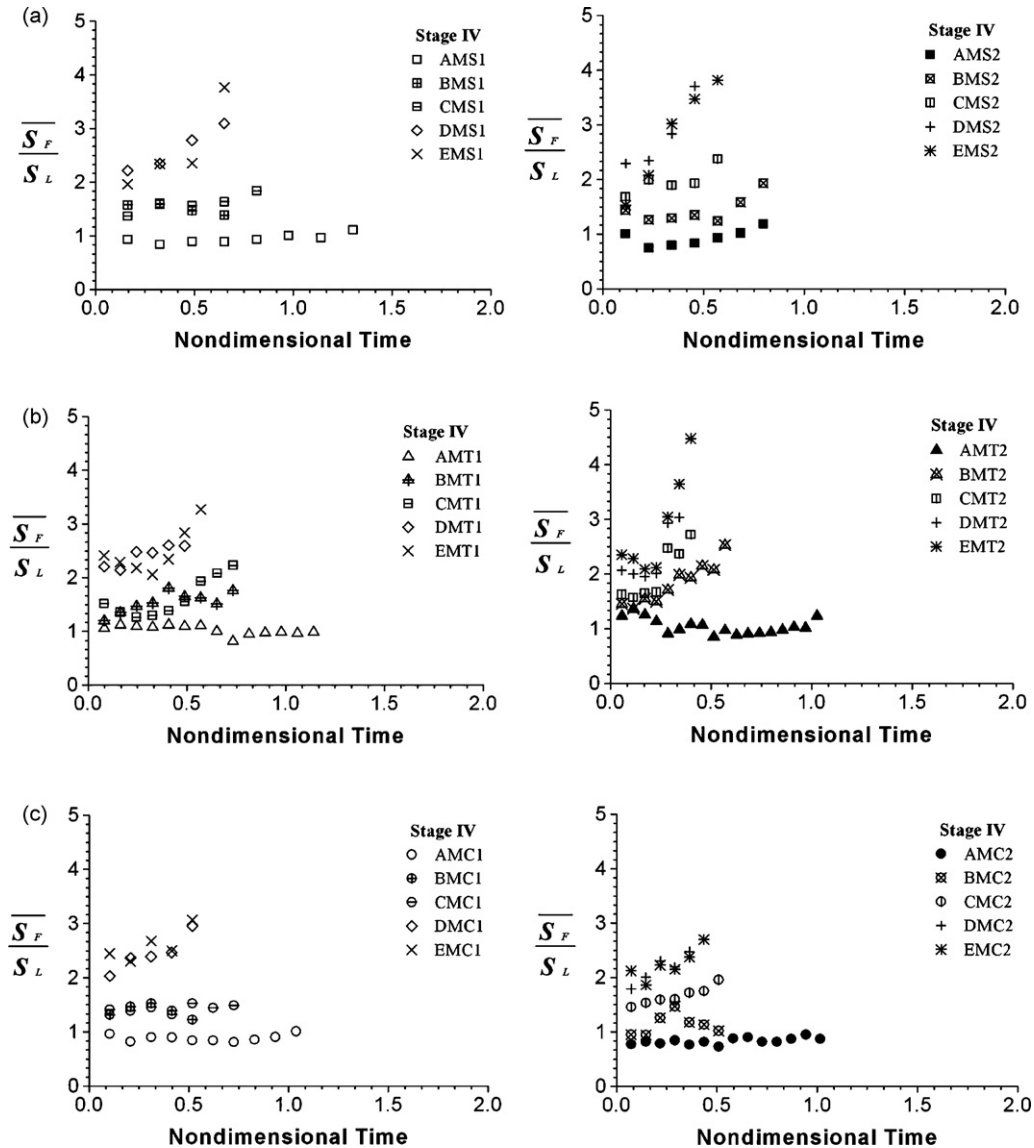
Fig. 8. The mean local flame speed during stage IV for multiple bars of 0.3 BR and 0.43 BR in the chambers with different *L/D* ratios: (a) square, (b) triangular and (c) circular.

the mean flame speed during these stages. However, the mean flame speeds for the higher blockage ratio of 0.43 during stage IV are higher than for 0.3. This implies that the larger obstruction during this stage causes more accelerating flame stretching and smaller decelerating regions in the wake of the obstructions than those of lower blockage ratios. However, the mean flame speed during state IV did not seem to increase much with blockage ratio compared to that published in the literature for large *L/D* ratios. This is due to different calculation methods for flame speed. The flame speeds measured in the literature used the tip of the flame front as a function of time or distance. The flame speeds presented, here, were measured over the whole of the flame front and include both accelerating and decelerating regions of the flame interaction with the obstacles.

The trends of $\bar{S}_F/S_L$ are similar for the three different obstacle types in chamber A. being around 1.0, regardless of the obstacle geometries and obstruction ratios. In chamber B, the flame interaction with the obstacles produces relatively higher flame speeds that are dependent on the obstacle geometry. The triangular and square cross-sections had higher values whereas the circular cross-section was still around 1.0. This is most probably due to lack of separation of the flow with the cylinders where as vortex shedding occurs with the other two geometries. Despite some fluctuations, the general trend in chambers of C–E is an increase in the flame speeds during the flame interaction with obstacles, the highest increase was obtained with the triangular obstacles of three presented at both obstruction ratios. It is clear that the flame speeds around the obstacles became sensitive to both the obstacle geometries and the obstruction ratios.

4.3. Pressure developments in different L/D ratios

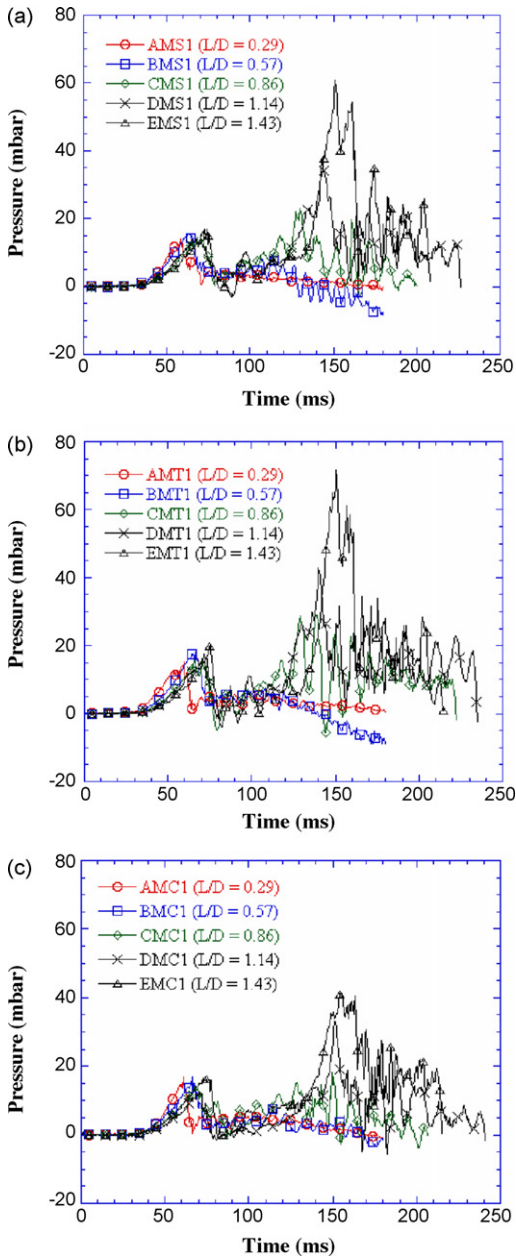The data for the maximum pressure, time to peak overpressures, time taken as flame emerges from each chamber and

Fig. 9. Pressure development in the five chambers for multiple bars of 0.3 BR: (a) square, (b) triangular and (c) circular.

Fig. 10. Pressure developments in the five chambers for multiple bars of 0.43 BR: (a) square, (b) triangular and (c) circular.

pressures at that time for all the obstacles in the chambers are shown in Table 5. The pressure in chambers A and B are very similar, with one peak occurring. However, two distinct pressure peaks (P_1 and P_2) occur in the other chambers.

The pressure–time curves are shown in Figs. 9 and 10 for blockage ratios of 0.3 and 0.43, respectively. The first peak in the pressure curve is related to the vent opening pressure, and the second peak is related to the overpressure generated by combustion in the chamber.

The first peak coincides in all chambers. The peak pressure in chamber A occurs during the flame interaction behind the central obstacle before the flame exits the chamber. However, the overpressure obtained in chamber B appears to occur as the flame approaches the obstacles, while other chambers, the first peak
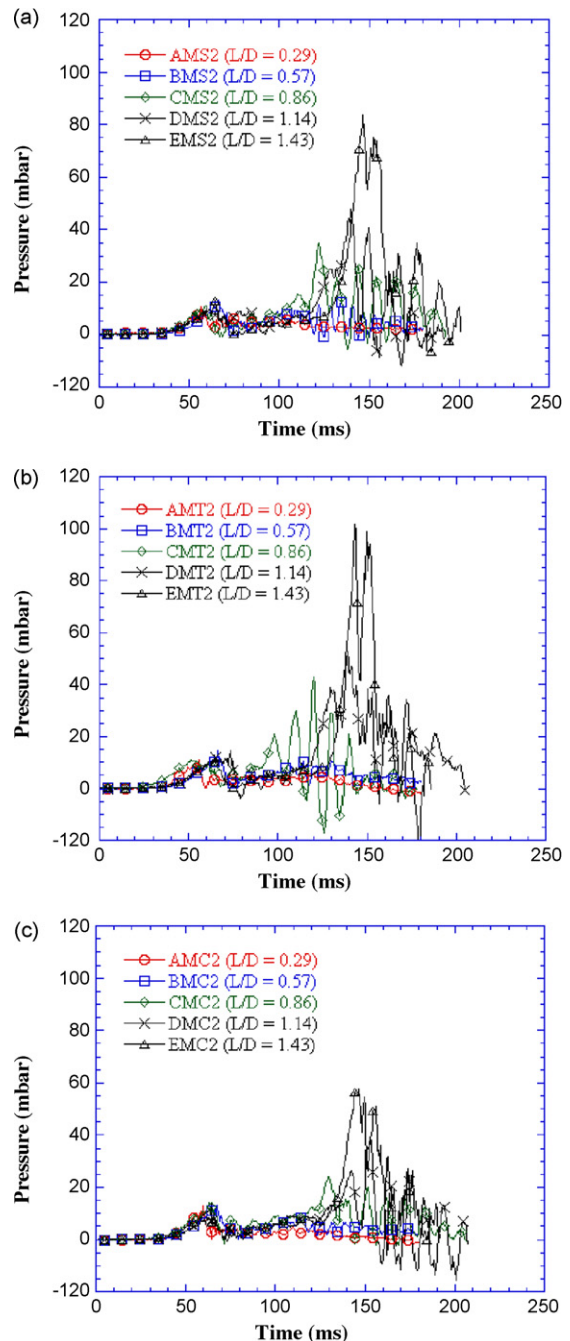
pressure occurs when the flame is located between the ignition and the obstacle. This strongly suggests that the first peak is associated with the destruction of the polyethylene over the vent rather than flame processes. The second peak pressure occurs as the flame front emerging from the vent ignites the unburned gas which has previously been expelled from the chamber, which results in a sharp increase in the internal pressure.

As the *L/D* ratio is increased, the trends in the data are similar for the first peak pressure, however, the second peak pressure increased. The overpressure in chambers A and B was unaffected by both the obstacle type and the obstruction ratio. However,

Table 5
The maximum pressure, time taken to the maximum peak pressure, time taken as flame emerges from each chamber, and pressure corresponding to that time for all obstacles within chambers

Chambers	Obstacles	P_1 (mbar)	T_1 (ms)	P_2 (mbar)	T_2 (ms)	FET (ms)	P_{FET} (mbar)
A	MS1	14	58.5	–	–	64	5
	MT1	15	58.5	–	–	64	4
	MC1	17	61	–	–	64	5
	MS2	11	56.5	–	–	64	3
	MT2	11	56	–	–	66	3
	MC2	13	60	–	–	64	3
B	MS1	16	63	–	–	96	3
	MT1	18	65	–	–	96	5
	MC1	17	66	–	–	96	3
	MS2	13	66.5	–	–	98	6
	MT2	15	66.5	–	–	96	5
	MC2	13	67.5	–	–	98	5
C	MS1	15	70.5	23	130	120	13
	MT1	16	65.5	29	129	116	13
	MC1	14	68	18	150	124	8
	MS2	11	59.5	35	122	116	11
	MT2	11	53.5	43	120	112	17
	MC2	14	63	24	130	120	12
D	MS1	14	68.5	38	143	140	23
	MT1	18	71.5	43	140	136	30
	MC1	13	71	33	154	144	10
	MS2	10	65	48	140	136	35
	MT2	18	73.5	53	137	132	47
	MC2	8	63	39	151	140	22
E	MS1	17	74	61	154	152	52
	MT1	20	75.5	71	150.5	148	61
	MC1	16	76	41	158	156	39
	MS2	13	64.5	84	151	148	67
	MT2	13	64	101	147	144	90
	MC2	14	64	57	154	152	49

FET: the time taken as flame emerges from the chamber; P_{FET}: pressure at FET.

with the larger chambers C–E there were significant differences in observed pressure with the triangular obstacles generating the highest overpressure and the cylindrical obstacles causing the lowest. For these chambers, the overpressure was highly sensitive to both the obstacle type and the obstruction ratio. This change in characteristics occurs between a L/D ratio of 0.57 and 0.86 and is related to higher flame speeds.

5. Conclusions

The investigations of interactions between flame and multiple obstacles within five chambers of different L/D ratios were presented. The main chamber was based on 1/30th scale chamber of a Korean Gas plant enclosure which has a low L/D ratio. The height of the chambers varied from 200 mm, and 1000 mm at 200 mm intervals. Three different multiple obstacles with cylindrical, triangular and square cross-sections were used. Two obstruction ratios of each obstacle type were employed: 0.3 BR and 0.43 BR. The main findings obtained from the investigations are given below.

1. The key finding of this work is that at L/D ratios > 0.86 the results for overpressure and flame speed regain consistency with those reported in the literature for the type of obstacles and blockage ratios used. Sharp-edged obstacle such as a triangular cross-section produced higher overpressures and flame speeds which also increased as the blockage ratio was increased. However, the results obtained at L/D ratios < 0.86, were different compared to those shown in literature. As explained in previous work [1], this is due to both the calculation method of flame speed and the different measurement system.

2. During stages I + II, then mean flame velocities were found to increase as the chamber height increased except for the two smallest L/D ratios of 0.29 and 0.57 where the flame velocities for the obstacles had a similar pattern. The flame velocities increased with the height of the chamber during stage III (square obstacles only). Stage IV resulted in the highest flame velocities. For the relatively small ratios of 0.29 and 0.57 the velocities during this stage were not significantly different. However, above 0.86 the flame velocity was sensitive to the obstacle type with the triangular obstacles causing the highest flame velocity and the cylindrical obstacle the lowest.

3. At the two smallest L/D ratios only one peak pressure was observed while at higher ratios two peak pressures were

observed. The first peak pressure was unaffected by both the obstacle geometries and the obstruction ratios. However, the second peak pressure was affected by both the obstacle geometry and the type of obstacle obstruction. Like the flame velocities, the triangular bar caused the highest pressure and the cylinder bars the lowest. The results showed that the flame development was correlated with the pressure development in the chambers having *L/D* ratios of 0.86–1.43.

References

[1] D.J. Park, A.R. Green, Y.S. Lee, Y.C. Chen, Experimental studies on interactions between a freely propagating flame and single obstacles in a rectangular confinement, Combust. Flame 150 (2007) 27–39.

[2] I.O. Moen, M. Donato, R. Knystautas, J.H.S. Lee, Flame acceleration due to turbulence produced by obstacles, Combust. Flame 39 (1980) 21–32.

[3] I.O. Moen, J.H.S. Lee, Pressure development due to turbulent flame propagation in large-scale methane–air explosions, Combust. Flame 47 (1982) 31–52.

[4] B.H. Hjertager, K. Fuhre, M. Bjorkhaug, Concentration effects on flame acceleration by obstacles in large-scale methane–air and propane–air vented explosions, Combust. Sci. Technol. 62 (1988) 239–256.

[5] H. Phylaktou, G.E. Andrews, Gas explosions in long closed vessels, Combust. Sci. Technol. 77 (1991) 27–39.

[6] M. Fairweather, G.K. Hargrave, S.S. Ibrahim, D.G. Walker, Studies of premixed flame propagation in explosion tubes, Combust. Flame 116 (1999) 504–518.

[7] A.R. Masri, S.S. Ibrahim, N. Nehzat, A.R. Green, Experimental study of premixed flame propagation over various solid obstructions, Exp. Therm. Fluid Sci. 21 (2000) 109–116.

[8] S.S. Ibrahim, A.R. Masri, The effects of obstructions on overpressure resulting from premixed flame deflagration, J. Loss Prev. Process Ind. 14 (2001) 213–221.

[9] S.S. Ibrahim, G.K. Hargrave, T.C. Williams, Experimental investigation of flame/solid interactions in turbulent premixed combustion, Exp. Therm. Fluid Sci. 24 (2001) 99–106.

[10] G.K. Hargrave, S.J. Jarvis, T.C. Williams, A study of transient flow turbulence generation during flame/wall interactions in explosions, Meas. Sci. Technol. 13 (2002) 1036–1042.

[11] F.N. Egolfopoulos, P. Cho, C.K. Law, Laminar flame speeds of methane–air mixtures under reduced and elevated pressures, Combust. Flame 76 (1989) 375–391.